

RESEARCH ARTICLE | JANUARY 08 2024

Adaptive powder nozzle setup for enhanced efficiency in laser metal deposition

Special Collection: [Proceedings of the International Congress of Applications of Lasers & Electro-Optics \(ICALEO 2023\)](#)

Annika Bohlen  ; Thomas Seefeld 



J. Laser Appl. 36, 012017 (2024)

<https://doi.org/10.2351/7.0001183>



CrossMark



Journal of
Laser Applications

[Learn More](#)



RAPID TIME
TO ACCEPTANCE



COMMUNITY
DRIVEN



EXPANSIVE
COVERAGE



PRESTIGIOUS
EDITORIAL BOARD



EXTENSIVE
MARKETING

Adaptive powder nozzle setup for enhanced efficiency in laser metal deposition

Cite as: J. Laser Appl. 36, 012017 (2024); doi: 10.2351/7.0001183

Submitted: 17 July 2023 · Accepted: 11 December 2023 ·

Published Online: 8 January 2024



Annika Bohlen¹ and Thomas Seefeld^{1,2}

AFFILIATIONS

¹BIAS—Bremer Institut für angewandte Strahltechnik GmbH, Klagfurter Str. 5, Bremen, 28359, Germany

²MAPEX Center for Materials and Processes—Universität Bremen, Bibliothekstraße 1, Bremen, 28359, Germany

Note: Paper published as part of the special topic on Proceedings of the International Congress of Applications of Lasers & Electro-Optics 2023.

ABSTRACT

Laser metal deposition (LMD) is a blown powder process used for the additive manufacturing of large and/or complex parts. The laser spot size is determined by the fiber optic cable and the imaging ratio of the process optics. Spot sizes typically used in LMD can range from 200 μm to several millimeters, whereby zoom optics can be employed to change the laser spot focus within seconds during the process. However, industrial powder nozzles are still static in terms of powder spot size. Changing the powder spot size in line with the laser spot size could ensure the favorable dual outcome of time savings when printing large volumes while also generating fine near-net-shape features. To help overcome the current limitations in the LMD process, this work examines an adaptive powder nozzle setup. In this discrete coaxial layout of three single lateral powder injectors, the individual powder injectors can be adjusted closer to or further from the process to, respectively, dilate or shrink the powder stream focus. Different inner diameters of powder injectors are hereby examined. The resulting powder propagation behavior is characterized for different setups of the single powder nozzles. Single beads are welded with different nozzle setups for fine and coarse powder spots, while the laser spot size is changed accordingly using zoom optics. The laser power is a closed-loop controlled by a two-color pyrometer to achieve comparative process temperatures. The single beads are evaluated with regard to their geometry. High-speed imaging provides supplementary information on weld bead generation.

Key words: laser metal deposition, powder nozzle, powder stream propagation

© 2024 Author(s). All article content, except where otherwise noted, is licensed under a Creative Commons Attribution (CC BY) license (<http://creativecommons.org/licenses/by/4.0/>). <https://doi.org/10.2351/7.0001183>

I. INTRODUCTION

Laser-based additive manufacturing is an increasingly important production technology for the processing of metallic materials.¹ It is a versatile process used to produce prototypes, end products, and various tools. For the technology to gain economic efficiency, the build-up rate is particularly crucial. Achieving a high build-up rate with little post-processing effort due to a near-net-shape geometry would enhance the productivity and thus the economic efficiency. Compared to laser powder bed fusion (LPBF), laser metal deposition (LMD) can allow significantly higher build-up rates, but it cannot yet match the high geometric flexibility and resolution of printed components produced by LPBF.²

The material feed in powder LMD is realized via a powder nozzle. Such nozzles are available in different types, including discrete nozzles, which have multiple powder streams, and continuous nozzles, which produce a single stream from an annular gap.³ The powder stream propagation plays an important role in the build-up efficiency of the LMD process. The LMD process is highly sensitive to a defocusing of the powder stream.^{4,5} A powder stream that is well-focused on the melt pool offers better catchment efficiency as well as more precise geometrical features.⁶

Adapting the powder nozzle and its powder propagation behavior to the weld bead requirements leads to cost and time savings. Thus, powder nozzle geometries, positions, and process parameters have been previously investigated. A smaller powder stream diameter can be achieved by using injectors with a smooth

25 January 2024 02:48:48

and wear-resistant inner surface.⁷ CFD simulations showed that shortening the convergence distance of the powder stream improves the stream's convergence.⁸ A decrease in the standoff distance by 1 mm (powder focus below the substrate surface) leads to a higher energy input into the deposited layer.⁹ Results have also shown that the amount of powder that interacts with the laser beam is highest at the specified working distance. An additional defocusing of the laser spot leads to a greater interaction between the powder and the laser beam.¹⁰ An increase in the nozzle axis angle from 25° to 35° and 45° inclination leads to lower powder capture efficiency and a decreased working distance stability, while a lower dispersion angle of the powder leads to a higher deposited layer height.¹¹ It has been observed that for discrete nozzles, larger particles have a higher dispersion angle.^{12,13} Experimental and numerical studies for a 4-jet discrete nozzle showed that a change in the injector's inner diameter from 3 to 2.4 mm leads to a decrease in the dispersion angle from a single injector, from 20° to 18° in the turbulence zone. A further decrease in the injector inner diameter to 1.8 mm increases the dispersion angle to 30° in the turbulence zone. This is assumed to be due to a decrease in the continuity of the gas flow velocity field, which leads to the divergence in the particle trajectory.⁹ Numerical studies for a 3-jet discrete nozzle showed a decrease in the powder focus size (where all three powder jets have merged) when reducing the injector inner diameter. A reduction from a 2.0 mm diameter to a 1.0 mm diameter led to a decrease in the powder focus spot from 5.9 to 2.4 mm, as well as an increase in the maximum particle velocity from 6.75 to 16.4 m/s, for a constant gas flow.¹²

The powder stream interacts with the laser beam and the melt pool to generate a weld bead. Results from investigations of cladding with a W-Cu powder mixture show that the different particles disappear into the melt pool at different times. Specifically, Cu particles, with a lower melting point, disappear into the melt pool after approximately 100 μ s, or after 300 μ m of floating on the melt pool. In contrast, the W particles float for longer.¹⁴ High-speed videos showing the cladding of Inconel 718 onto stainless steel 316 substrate with a continuous nozzle revealed three different zones for powder catchment behavior. In the solidified region, the particles ricochet. In the region of the melt pool outside the laser spot, the particles can be incorporated or adhere to the surface, where they can also incorporate after some time or move to the solidified zone and become part of the weld bead roughness. The third zone is the melt pool in the laser beam, where particles are readily incorporated; in this case, they can move radially inwards, which is assumed to be due to the Marangoni flow.⁶ The findings from the laser beam welding of AISI 316L showed that the direction of the Marangoni flow can change with temperature. The point at which the sign of the temperature gradient of surface tension changes is approximately 2550 K.¹⁵ CFD simulations for laser DED processes suggested that the impingement of a particle is the main driving force for fluid motion in the melt pool, making Marangoni forces less significant. The flow pattern is believed to be highly oscillatory, chaotic and random.¹⁶ High-speed x-ray imaging of LMD with titanium powder showed that pores are moved by the melt flow, which is driven by delivered particles and Marangoni flow. This study also showed that particles entering the melt pool with a high velocity can generate space behind them, leading to pore formation.¹⁷ In

the LMD of AISI 316L, experiments showed that the incorporation time of particles directly in the laser beam is around 0.2 ms, increasing toward 0.4 ms at the edge of the melt pool. Additional model calculations suggested that the surface-tension-driven wetting mechanism can lead to a rising of particles from the melt pool due to temperature differences after the initial melt pool contact.¹⁸

This paper focuses on how weld bead generation is influenced by the distance of the injector opening to the working plane as well as the injector's inner diameter. With a laboratory setup of three lateral injectors, different nozzle setups can be applied. The powder stream propagation from each nozzle setting is characterized. The geometrical features of the bead, such as the width, height, and depth, are evaluated. Additionally, the findings are related to high-speed video recordings of the processes.

II. EXPERIMENTAL SETUP AND METHODS

A. Adaptive nozzle system

The laboratory setup for the adaptive nozzle system consisted of a central shielding gas nozzle with an opening of 7 mm and three lateral ceramic tubes that served as the injector nozzles (see Fig. 1). The inclination angle of the three injectors was 23° with respect to the vertical, and they were positioned circularly at a distance of 120° around the coaxial laser beam. The injector's inner diameter could be adjusted from $d = 1$ mm to $d = 1.7$ mm. The distance from the injector opening to the origin of the coordinate system varied between $l = 10$ mm and $l = 14$ mm. Thus, four different nozzle setups could be investigated. The powder injectors were sputtered with gold to protect them from reflective laser radiation.

B. Powder and powder stream characterization

The powder material was gas-atomized AISI 316L with a nominal particle size of $+106 \mu\text{m} - 45 \mu\text{m}$, sourced from the manufacturer Deutsche Edelstahlwerke Specialty Steel GmbH & Co. KG. The sieve analysis from the manufacturer is presented in Table I.

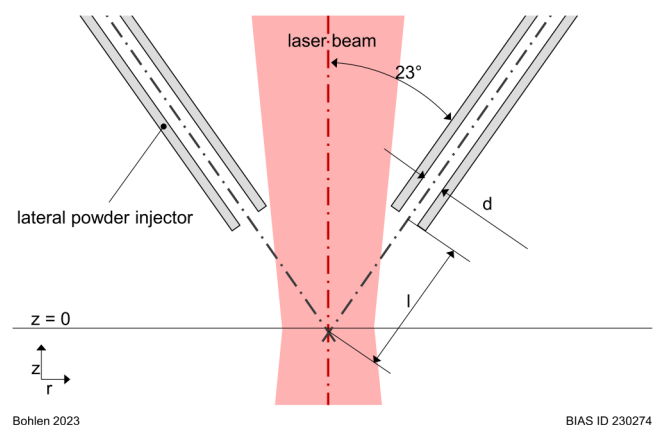


FIG. 1. Laboratory setup comprising three lateral powder injectors for different injector inner diameters d and distances to origin l .

25 January 2024 02:48:48

TABLE I. Sieve analysis of the AISI 316L powder from the manufacturer.

<38 μm %	38–45 μm %	45–53 μm %	53–63 μm %	63–90 μm %	90–106 μm %	106–125 μm %	>125 μm %
0.0	1.7	15.5	16.5	49.3	16.9	0.1	0.0

The SEM image (Fig. 2) of the powder shows that the powder particles are mainly spherical with satellite particles. Some particles show an irregular shape and surface.

To characterize the nozzle setups, single horizontal layers of the powder stream were illuminated with a line laser and recorded at a distance of 0.5 mm (see Fig. 3). For each recorded layer, a powder stream radius was calculated via a radial-symmetrical representation of the powder distribution in each layer. Concentric circles around the center of the nozzle were evaluated with regard to their intensity. A mean intensity was calculated for each concentric circle, for use in calculating an equivalent powder spot diameter. The chosen method was to set the boundary of the powder spot to where the intensity had fallen to 14% of the maximum measured mean intensity. This method is similar to the D86 method used in laser beam measurements. A more detailed description of this method for characterizing the powder stream can be found in Refs. 19 and 20.

C. Experiments

A LUNOVU 835 LMD machine equipped with a Laserline LDF 4000-40 diode laser with wavelengths between 960 and 1040 nm was used, in addition to a Laserline OTZ-5 Zoom Optics with a 400 μm laser light cable. Through the optics, a top hat profile was obtained in focus with a laser spot size between 1.2 and 4 mm. The processing head was stationary and the substrate with the machining table moved. A BLC twin powder feeder was used to transport the powder. Argon was used as a carrier gas and shielding gas.

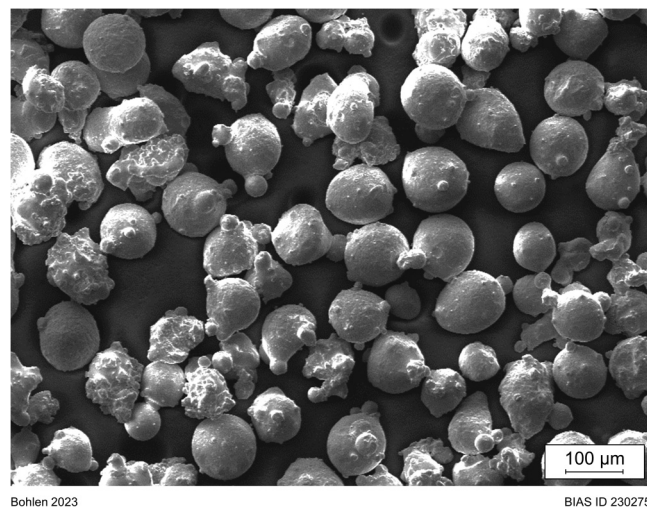


FIG. 2. SEM image of the AISI 316L powder.

S235 structural steel was used as the substrate material. The substrates were 100 mm in length, 30 mm in width, and 20 mm in height. The substrate surface was sandblasted. The process velocity was set to 0.8 m/min. The powder mass flow rate was set to 10 g/min. The carrier gas flow rate was set to 5 l/min, and the shielding gas flow rate was set to 10 l/min. Five different laser spot sizes were used, namely, 1.6, 2.3, 2.8, 3.2, and 3.6 mm, all in focus with a top-hat laser power intensity distribution, leading to an increase in the laser spot area by a factor of 5. Each parameter set was welded three times on room-temperature substrates and analyzed. The standard deviation was calculated from the three experiments per parameter set.

After manufacturing, the samples were metallographically prepared as cross sections to measure the width, height, and depth of the welded bead in the middle of the weld track. Cross sections were etched with Nital for 10 s. The powder catchment efficiency was calculated from the metallographic cross sections. For this purpose, the area of the weld bead above the substrate surface was measured using STEAM ENTERPRISE software from Olympus. The size of the area for 100% powder catchment efficiency was also calculated. Assuming an AISI 316L density of 8 kg/dm³ and considering a process velocity of 0.8 m/min and a powder mass flow rate of 10 g/min, the deposited volume per mm was 1.56 mm³/mm. Based on the assumption that this value represents 100% powder catchment efficiency, it was possible to calculate the powder catchment efficiency and deposition rate for all experiments. To calculate the dilution, the measured total melted area was divided by the measured area beneath the substrate surface.

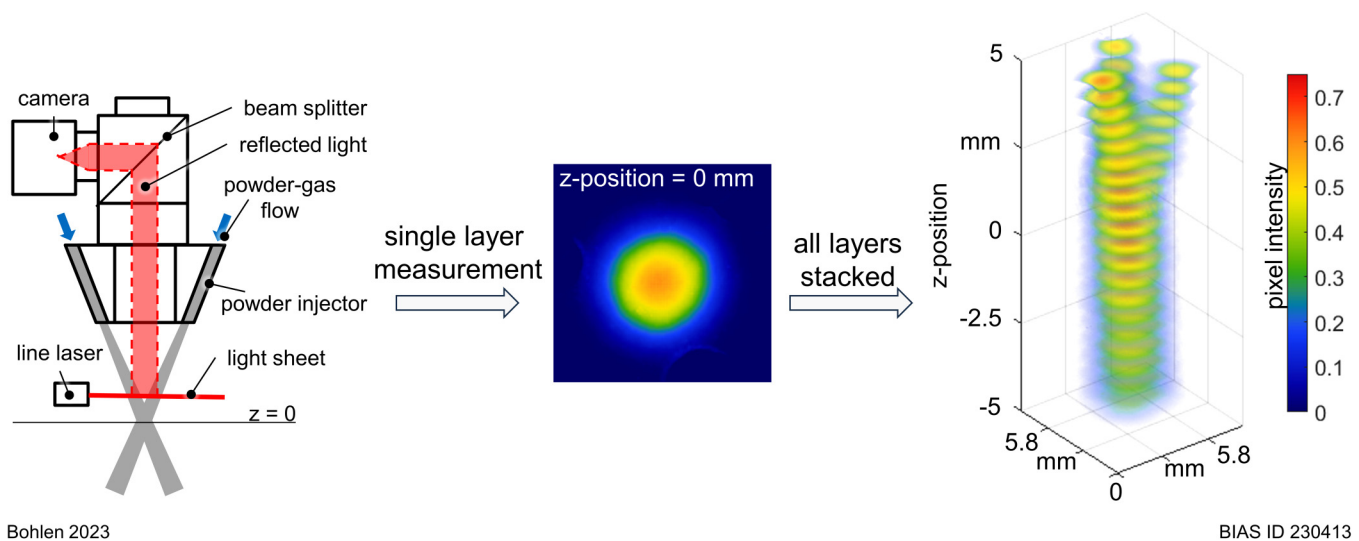
D. Pyrometer closed-loop control

A Sensortherm Metis H322 two-color pyrometer with a measuring range between 700 and 2300 °C was integrated coaxially for the closed-loop control of the laser power. The pyrometer was connected to the optics through the camera output located below the collimation of the optics. It was moved together with the laser beam to monitor the temperature of the process zone and control the laser power accordingly. The measuring spot of the pyrometer was approximately 4 mm in diameter. The pyrometer was not specifically calibrated with the used optics. The laser power was a closed-loop controlled by the pyrometer to a set pyrometer measurement value of 1200 (arbitrary unit, not calibrated to the centigrade scale). The signal from the controller to the laser was recorded with an oscilloscope in Volts. The used power could be evaluated based on a power measurement. Both the measured pyrometer data and the laser power were averaged over the process time (excluding the first and last 0.1 s), and standard deviations were calculated.

E. High-speed imaging

An i-Speed 7 high-speed camera from iX Cameras was used to capture high-speed videos with a frame rate of 75 and 45 kHz to

25 January 2024 02:48:48



Bohlen 2023

BIAS ID 230413

FIG. 3. Measurement of single horizontal layers of the powder stream illuminated with a line laser. Left: schematic of laboratory setup; middle: single layer measurement in false colors; right: stacked layers of measurement from nozzle setup $d = 1.7$ mm and $l = 10$ mm.

respectively observe the powder entering the melt pool and ejected from the powder injector. All videos were illuminated using a Cavilux illumination laser from Cavitax. Particle tracking was done with TrackMate²¹ within IMAGEJ software.

To analyze the powder particles entering the melt pool, the recording parameters were the laser spot sizes of 1.6, 2.8, and 3.6 mm for all nozzle setups. Within 2000 frames, 100 particles that entered the melt pool were randomly selected and tracked through multiple frames to gain knowledge about their interaction times with the melt pool surface. They were separated into particles that entered the melt pool immediately and those that remained on the melt pool surface for multiple frames. Tracking was not performed for the laser spot size 3.6 mm since the melt pool was not sufficiently situated within the frame of the recording.

For the powder particles ejected from the powder injector, automated particle detection was possible. 1000 particles were tracked to calculate the particles' mean velocity. The local distribution of the particles was needed to calculate the dispersion angle. For this purpose, a background model consisting of 500 frames was created. After subtracting this background model from the current frame, it was possible to obtain a binarized image of the particles. These images were summed up to create an intensity map of the particles' locations over 10 000 frames. At a distance of 10 mm to the injector exit, the intensity along a parallel line to the exit was extracted. A Gaussian fit was calculated for this intensity, whereby $1/e^2$ marked the boundary of the powder stream. The dispersion angle was calculated from this boundary to the injector exit, as shown in Fig. 4.

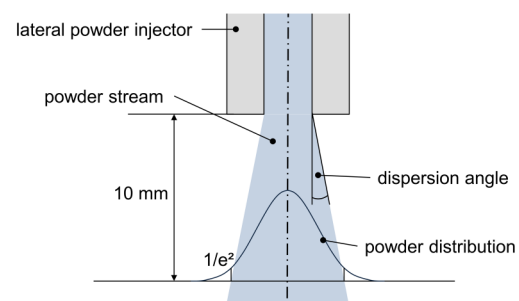
III. RESULTS

The calculated powder stream radii with varied distances to the nozzle exits are shown in Fig. 5. It can be seen that regardless

of the distance and diameter of the ceramic powder inlets, the waist of the powder streams is at the same z -position for all nozzle setups.

During the process, the closed-loop controlled laser power needed to achieve the set pyrometer measurement value of 1200 was recorded. Figures 6 and 7 show the mean pyrometer measurement data throughout the process. It can be seen that the set pyrometer measurement data are reached and maintained throughout the process (the standard deviation is smaller than the marker in all cases). The laser power needed to achieve these values rises almost linearly from laser spot sizes of 1.6–2.8 mm in all four nozzle setups. For the nozzle setups with an inner diameter of 1 mm (Fig. 7), the required laser power stagnates for the 2.8 and 3.6 mm laser spot diameters.

Since the laser power was a closed-loop controlled for a stable process zone temperature, the resulting laser power densities are



Bohlen 2023

BIAS ID 230276

FIG. 4. Explanatory sketch of the dispersion angle.

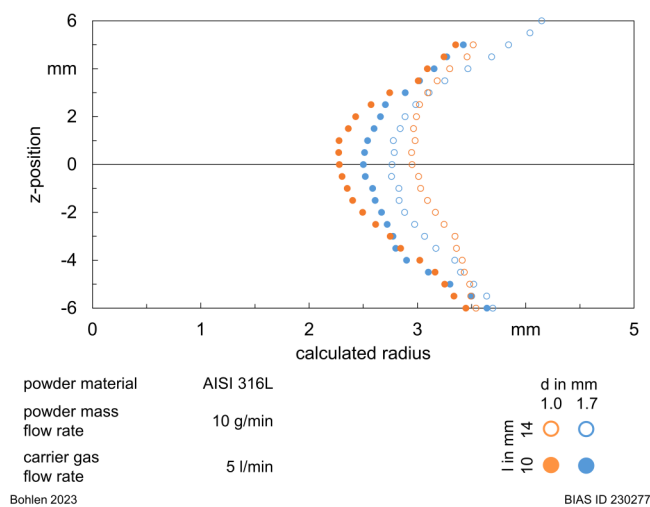


FIG. 5. Calculated radii in relation to the distance to the powder nozzle exit for different injector inner diameters.

different for the different laser spot sizes and nozzle setups; see Fig. 8. The laser power density decreases with increasing laser spot size. The lowest densities can be observed for the nozzle setup $d = 1.0$ mm; $l = 14$ mm.

Examples of metallographic cross sections for all four nozzle setups and the five different laser spot sizes can be seen in Fig. 9. The different welding depths are prominent, and an irregular welding depth can be particularly observed for the nozzle setups with a small distance to the substrate and a 1.7 mm inner diameter. Nozzle setups with smaller injector diameters show more pores.

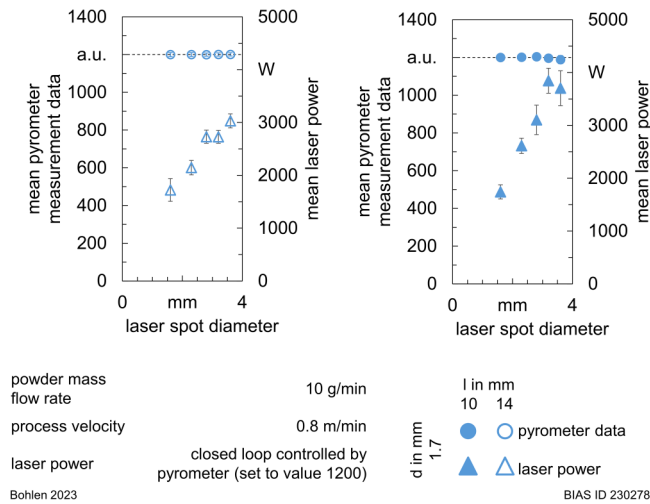


FIG. 6. Pyrometer measurement data measured by two-color pyrometer with active closed-loop control of laser power to a preset value of 1200 for inlets with a 1.7 mm inner diameter.

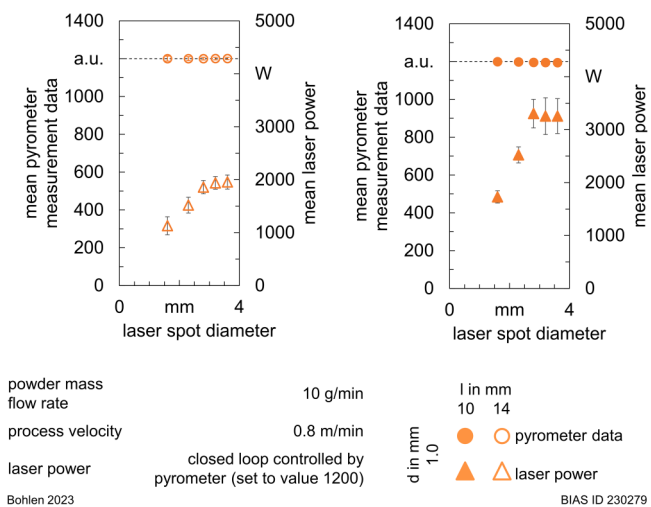


FIG. 7. Pyrometer measurement data by two-color pyrometer with active closed-loop control of laser power to preset value of 1200 for inlets with 1.0 mm inner diameter.

The calculated powder catchment efficiency and deposition rate are shown in Fig. 10. A higher powder catchment efficiency can be seen for powder injectors closer to the substrate (solid markers compared to open markers). Here, it can be seen that with increasing laser spot size, the efficiency first rises but then decreases. The lowest powder catchment efficiency is recorded for the small-diameter nozzle with a larger distance to the substrate.

The bead height measured from the cross sections is shown in Fig. 11. Solid markers show the weld bead height for powder

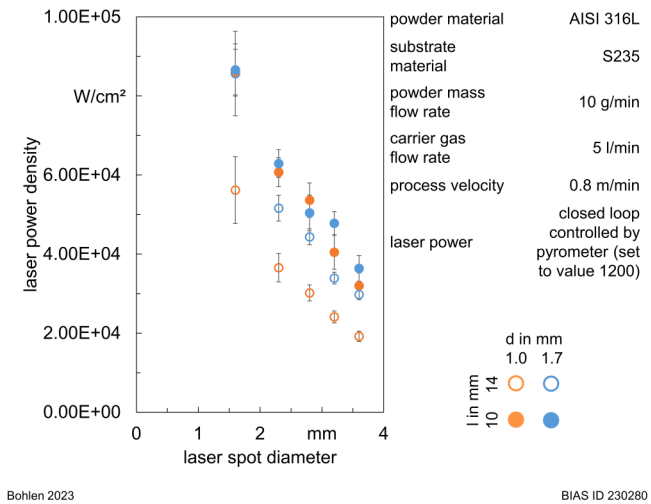


FIG. 8. Laser power density in relation to the laser spot diameter for different nozzle setups with controlled laser power.

25 January 2024 02:48:48

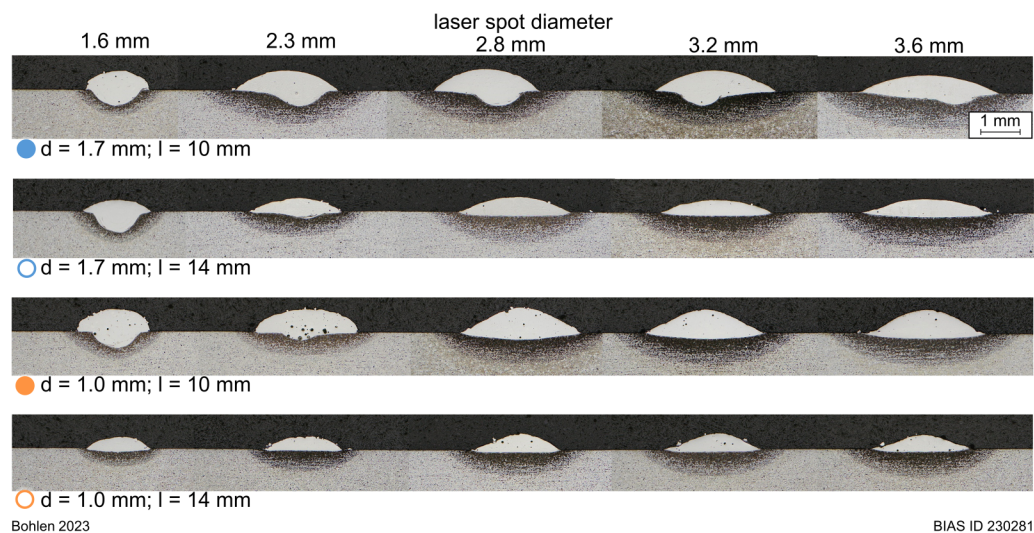


FIG. 9. Cross sections of each nozzle setup with five different laser spot sizes.

injectors closer to the substrate. These values are distinctly higher compared to open markers, representing the powder injectors further away from the substrate. While the deposited height from the longer distance to substrate nozzles is almost the same for both injector inner diameters, the nozzle that is closer to the substrate and has an inner diameter of 1 mm generates the highest weld beads for all laser spot diameters (solid lighter markers).

Figure 12 shows the measured width of the welded beads. An almost linear trend can be observed for all four nozzle setups, whereby the width increases for larger laser spot diameters. For the

smallest laser spot diameter of 1.6 mm, the bead width of all four variations is just under 2 mm. For the largest laser spot diameter of 3.6 mm, the narrowest bead with a width of 2.6 mm is achieved with a nozzle setup of a large distance to the substrate and a 1 mm injector inner diameter; the highest width of 3.4 mm is found for a nozzle setup of an 1.7 mm inner diameter and a small distance to the substrate. Note that for the smallest laser spot diameter (1.6 mm), the width is higher than the spot diameter, while for the largest laser spot diameter (3.6 mm), the achieved width is smaller than the laser spot diameter.

25 January 2024 02:48:48

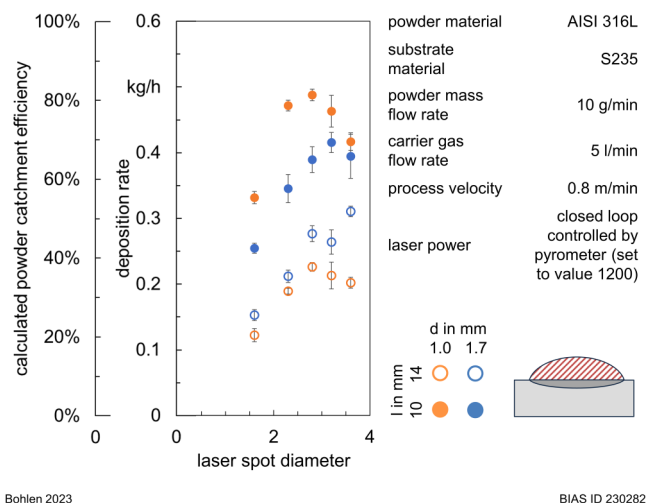


FIG. 10. Calculated powder catchment efficiency and deposition rate in relation to the laser spot diameter for all nozzle setups.

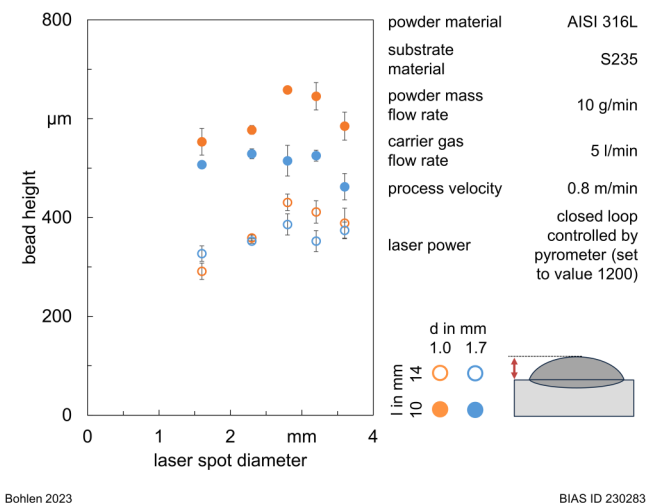
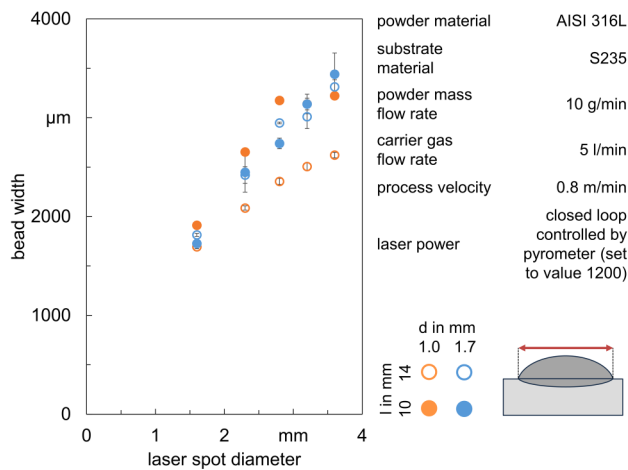


FIG. 11. Height measurement of welded beads for all nozzle setups in relation to the laser spot diameter.



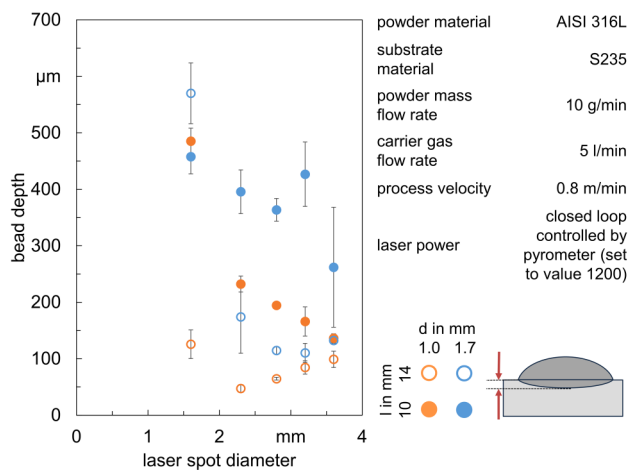
Bohlen 2023

BIAS ID 230284

FIG. 12. Width measurement of welded beads for all nozzle setups in relation to the laser spot diameter.

The measured bead depth is shown in Fig. 13. All nozzle setups, excluding $d = 1.0$ mm; $l = 14$ mm, show a decreasing bead depth with increasing laser spot size. For every nozzle setup, the smallest laser spot diameter leads to the highest bead depth. The highest bead depths can be observed for $d = 1.7$ mm; $l = 10$ mm.

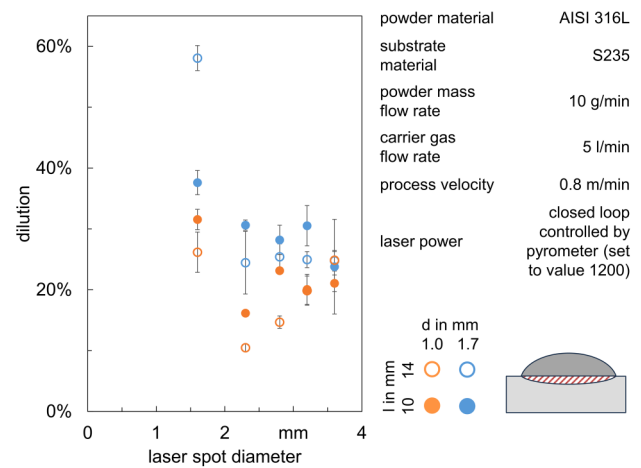
The dilution of the weld beads was calculated (see Fig. 14). The highest dilution for all nozzle setups is found for the 1.6 mm laser spot size. The larger diameter nozzle ($d = 1.7$ mm) shows a decreasing trend in dilution with increasing laser spot size. The smaller diameter nozzles (lighter markers) show overall lower dilution than the larger diameter ones.



Bohlen 2023

BIAS ID 230285

FIG. 13. Welding depth measurement of welded beads for all nozzle setups in relation to the laser spot diameter.



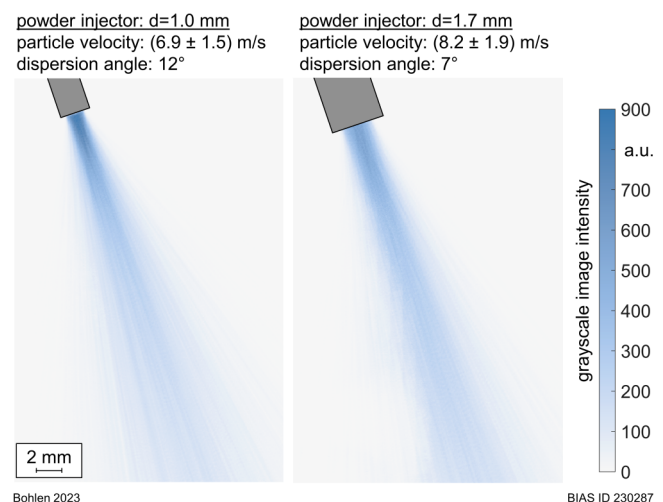
Bohlen 2023

BIAS ID 230286

FIG. 14. Dilution of welded beads for all nozzle setups in relation to the laser spot diameter.

The high-speed recordings of the particles ejected from the powder injectors permit the calculation of particle velocity and dispersion angle (Fig. 15). The velocity for particles from the larger injectors ($d = 1.7$ mm) is higher $[(8.2 \pm 1.9) \text{ m/s}]$ than for the smaller injectors $[(6.9 \pm 1.5) \text{ m/s}]$. The dispersion angle is larger for the injector with a smaller inner diameter ($d = 1$ mm), at 12° compared to 7° for $d = 1.7$ mm.

The interaction of the particles with the melt pool was observed via high-speed recordings, and single frames from the process can be seen in Fig. 16. This example shows a particle that lands on the melt pool at $t = 0.0 \mu\text{s}$ and shortly thereafter



Bohlen 2023

BIAS ID 230287

FIG. 15. Summed-up image of detected particles from 10 000 frames.

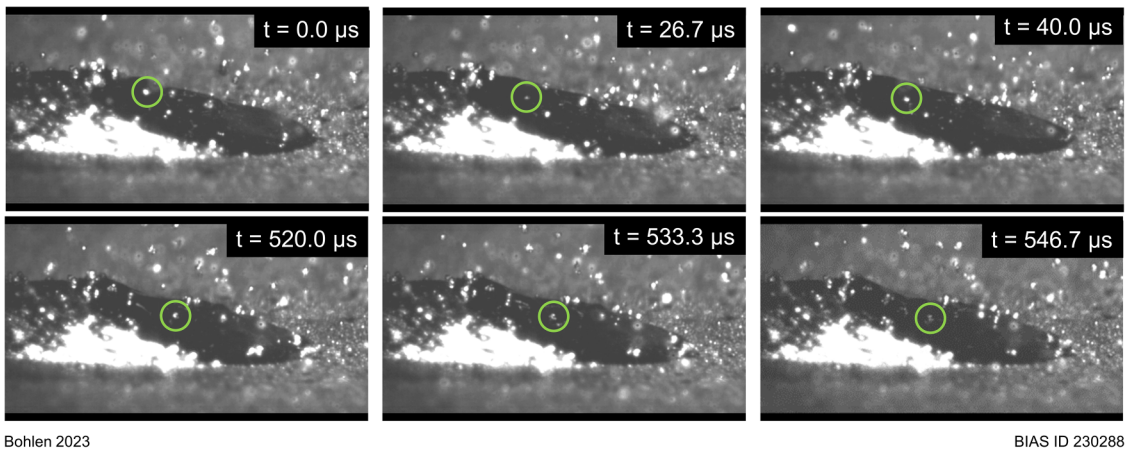


FIG. 16. Single frames from a high-speed recording of the LMD process with a laser spot size of 1.6 mm and the nozzle setup $d = 1.7$ mm; $l = 10$ mm.

submerges beneath the melt pool surface ($t = 26.7 \mu\text{s}$), re-emerging directly after ($t = 40.0 \mu\text{s}$). It then travels toward the center of the melt pool, and after $546.7 \mu\text{s}$ is fully incorporated into the melt pool.

The particles incorporated into the melt pool can be separated into two groups: particles that are instantly incorporated into the melt pool and particles that float on the melt pool surface for several μs . The percentage of floating particles can be seen in Fig. 17. The highest number of floating particles can be observed for the nozzle setup $d = 1.0$ mm; $l = 10$ mm. The highest fraction was 75% at a laser spot size of 2.8 mm.

The direction in which the floating particles moved was also evaluated, and the results are depicted in Fig. 18. The particles

either remain stationary or float toward the edge of the melt pool or towards the center of the melt pool. In all cases, most particles remain stationary (60% to 90%). With an increasing laser spot size, the amount of stationary floating particles increases as well, except for the nozzle setup $d = 1.0$ mm; $l = 14$ mm.

The time each tracked particle remained on the melt pool surface was analyzed as well. Since individual particles may remain on the surface for a lot longer than the average particle, box plots are used to show the median value, upper and lower quartiles, whiskers, and outliers; see Fig. 19. The distance between the upper and lower quartiles is the interquartile range (IQR). Outliers are values that are more than $1.5 \cdot \text{IQR}$ away from the upper and lower quartiles. Whiskers connect the upper and lower quartiles to the

25 January 2024 02:48:48

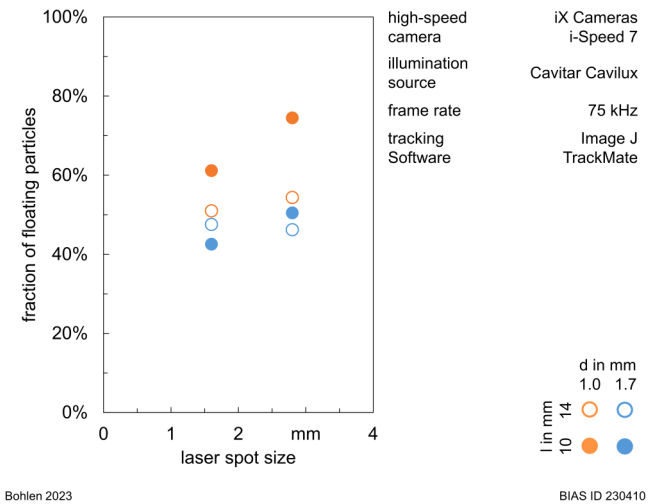


FIG. 17. Percentage of particles that land on the melt pool compared to those that float on the melt pool for several μs .

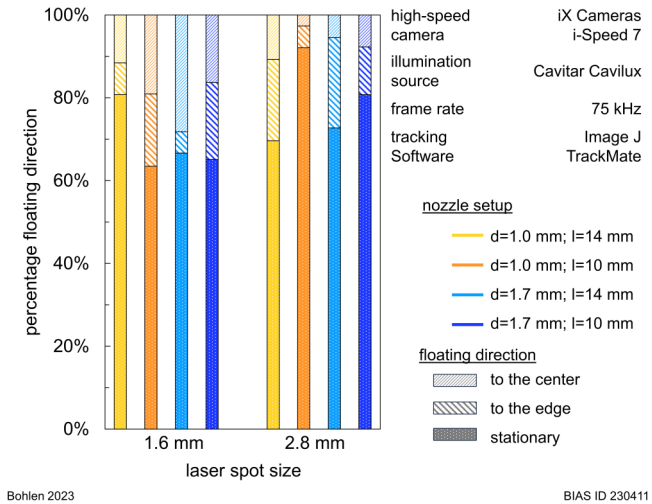


FIG. 18. Percentage of floating particles that are either stationary or floating towards the center of the melt pool or the edge of the melt pool.

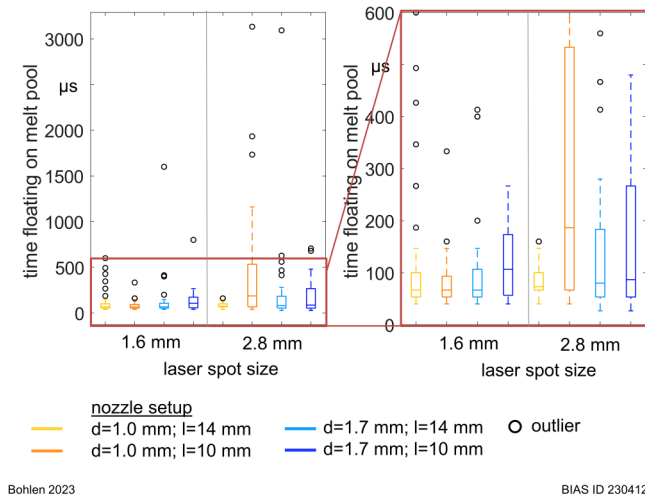


FIG. 19. Box plots showing the time individual tracked particles float on the melt pool before incorporation.

nonoutlier maximum and minimum. For the nozzle setup $d = 1.0$ mm; $l = 14$ mm, no distinct difference in floating time can be seen, except for the number of outliers. In all other setups, the larger laser spot size leads to higher 25th and 75th percentiles, correlating with longer floating times.

IV. DISCUSSION

The injector's inner diameter of 1.7 mm has a smaller powder stream focus radius if the injectors are closer to the reference plane, which is due to the dispersion angle of the powder. Compared to the smaller distance to the reference plane, the larger distance to the reference plane produces beads with a similar width (Fig. 12), but a lower height (Fig. 11). This is due to a smaller number of particles reaching the melt pool, which is supported by the higher powder catchment efficiency for the smaller distance to the reference plane (Fig. 10). For both distances to the reference plane, the

number of floating particles before incorporation into the melt pool is nearly the same, but the particles from the nozzle setup with a smaller distance float on the melt pool for longer (Fig. 19). As yet, no explanation for this phenomenon has been found, and further investigation is required.

A reduction of the injector's inner diameter to 1.0 mm leads to a change in the powder stream radius. The smaller distance to the reference plane for this diameter has a smaller powder stream radius compared to the larger diameter with the same distance. This is in agreement with the findings of Li *et al.*¹² The larger distance to the reference plane leads to a larger powder stream radius, if compared to the larger diameters. This is most likely due to the dispersion angle of the powder. Since the inner diameter of the injectors is smaller, the powder stream is also smaller directly after the injector opening. However, the higher dispersion angle (Fig. 15) results in a faster-growing powder spot size along the injector axis compared to the larger injector diameters. This leads to the assumption that the injector diameter should not be decreased under a certain threshold, since this would cause the dispersion of the powder to become larger. Comparable results were found by Yao *et al.*⁹ Their findings were that the decrease in injector's inner diameter from 3 to 2.4 mm leads to a decrease in the dispersion angle from a single injector, from 20° to 18° in the turbulence zone. A further decrease in the injector inner diameter to 1.8 mm increases the dispersion angle to 30° in the turbulence zone. An explanation for this could be an enhanced interaction between the injector wall and the particles. Each contact will slow down a particle. This is in agreement with so lower particle velocity for smaller inner injector diameter measured in this work (see Fig. 15). If more collisions occur there is a higher probability that a particle has a wall collision close to the injector exit, leading the particle to exit at a wider angle. This is in agreement with the larger dispersion angle measured in Fig. 15.

An increase in the laser spot size leads to a larger melt pool that can incorporate more powder since the powder stream spot is larger than the laser spot diameter. This leads to a decrease in the laser power density since more powder absorbs the laser energy, thus increasing the overall laser coupling efficiency of the process. With a larger laser spot size, more particles that are incorporated into the melt pool float before incorporation (Fig. 17). Also, with

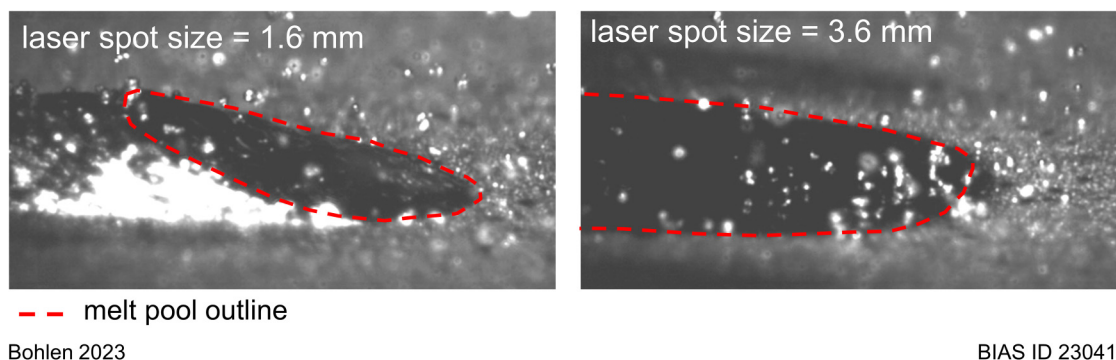


FIG. 20. Single frames from a high-speed recording of the LMD process with laser spot sizes 1.6 mm and 3.6 mm and the nozzle setup $d = 1.7$ mm; $l = 10$ mm.

increasing laser spot size, fewer particles move while floating (Fig. 18) but remain stationary on the melt pool surface for longer (Fig. 19). This can be seen especially at the front of the melt pool; see Fig. 20.

A lifting of particles from the melt pool after the initial contact, as described in Ref. 18, can be seen for the duration of one frame, followed by a long floatation time (Fig. 16). These long times seem to be outliers, but they might be explained by a small absolute number of larger powder particles. Larger particles, which have a higher mass, heat up more slowly, thereby slowing their melting and incorporation. Note that, assuming an ideal spherical shape, the calculated mass of a particle with a diameter of $106\text{ }\mu\text{m}$ is roughly 13 times the mass of a $45\text{ }\mu\text{m}$ particle. To gain more insight into the effect of large particle size, more particles should be traced per process.

V. CONCLUSION

The interactions between the powder stream, laser beam and melt pool and the subsequent impact on the weld bead were investigated using a laboratory nozzle setup. The following conclusions can be drawn:

- The injector diameter has a significant impact on the particle velocity and dispersion angle. A larger inner diameter of $d = 1.7\text{ mm}$ leads to a higher particle velocity of $(8.2 \pm 1.9)\text{ m/s}$ and a smaller dispersion angle of 7° compared to a smaller inner diameter of $d = 1\text{ mm}$. For the smaller inner diameter a particle velocity of $(6.9 \pm 1.5)\text{ m/s}$ is achieved and a dispersion angle of 12° .
- With the small injector diameter of $d = 1\text{ mm}$, a small powder stream radius can be achieved, for which a small distance to the reference plane is necessary.
- For an adaptive nozzle system, a large applicable field of working distances is needed. This can be achieved by using a larger injector diameter nozzle, which has a more stable welding result with different distances to the reference plane.

ACKNOWLEDGMENTS

This work was funded by the Deutsche Forschungsgemeinschaft (DFG, German Research Foundation)—Project No. 424886092 (Adaptive powder nozzle for additive manufacturing processes). LUNOVU 835 LMD-Machine is funded by the Deutsche Forschungsgemeinschaft (DFG, German Research Foundation)—Project No. 434424600 (Highly flexible material synthesis and microstructure adjustment through combined laser deposition welding and short-term heat treatment for high-throughput materials development).

AUTHOR DECLARATIONS

Conflict of Interest

The authors have no conflicts to disclose.

Author Contributions

Annika Bohlen: Data curation (equal); Investigation (equal); Methodology (equal); Visualization (equal); Writing – original

draft (equal). **Thomas Seefeld:** Project administration (equal); Supervision (equal); Writing – review & editing (equal).

REFERENCES

- ¹M. Schmidt, M. Merklein, D. Bourell, D. Dimitrov, T. Hausotte, K. Wegener, L. Overmeyer, F. Vollertsen, and G. N. Levy, “Laser based additive manufacturing in industry and academia,” *CIRP Ann.* **66**, 561–583 (2017).
- ²T. Petrat, B. Graf, A. Gumenyuk, and M. Rethmeier, “Laser metal deposition as repair technology for a gas turbine burner made of Inconel 718,” *Phys. Proc.* **83**, 761–768 (2016).
- ³A. Guner, P. Bidare, A. Jiménez, S. Dimov, and K. Essa, “Nozzle designs in powder-based direct laser deposition: A review,” *Int. J. Precis. Eng. Manuf.* **23**, 1077–1094 (2022).
- ⁴G. Zhu, D. Li, A. Zhang, G. Pi, and Y. Tang, “The influence of laser and powder defocusing characteristics on the surface quality in laser direct metal deposition,” *Opt. Laser Technol.* **44**, 349–356 (2012).
- ⁵S. Zekovic, R. Dwivedi, and R. Kovacevic, “Numerical simulation and experimental investigation of gas–powder flow from radially symmetrical nozzles in laser-based direct metal deposition,” *Int. J. Machine Tools Manuf.* **47**, 112–123 (2007).
- ⁶H. Siva Prasad, F. Brueckner, and A. F. H. Kaplan, “Powder catchment in laser metal deposition,” *J. Laser Appl.* **31**, 22308 (2019).
- ⁷A. Haghshenas, A. Bohlen, D. Tyralla, and R. Groll, “The relevance of wall roughness modeling for simulation of powder flows in laser metal deposition nozzles,” *Int. J. Adv. Manuf. Technol.* **123**, 1441–1458 (2022).
- ⁸S. Takemura, R. Koike, Y. Kakinuma, Y. Sato, and Y. Oda, “Design of powder nozzle for high resource efficiency in directed energy deposition based on computational fluid dynamics simulation,” *Int. J. Adv. Manuf. Technol.* **105**, 4107–4121 (2019).
- ⁹X. X. Yao, J. Y. Li, Y. F. Wang, X. Gao, T. Li, and Z. Zhang, “Experimental and numerical studies of nozzle effect on powder flow behaviors in directed energy deposition additive manufacturing,” *Int. J. Mech. Sci.* **210**, 106740 (2021).
- ¹⁰M. Mazzarisi, V. Errico, A. Angelastro, and S. L. Campanelli, “Influence of standoff distance and laser defocusing distance on direct laser metal deposition of a nickel-based superalloy,” *Int. J. Adv. Manuf. Technol.* **120**, 2407–2428 (2022).
- ¹¹J. C. Haley, B. Zheng, U. S. Bertoli, A. D. Dupuy, J. M. Schoenung, and E. J. Lavernia, “Working distance passive stability in laser directed energy deposition additive manufacturing,” *Mater. Des.* **161**, 86–94 (2019).
- ¹²L. Li, Y. Huang, C. Zou, and W. Tao, “Numerical study on powder stream characteristics of coaxial laser metal deposition nozzle,” *Crystals* **11**, 282 (2021).
- ¹³A. Bohlen, D. Tyralla, and T. Seefeld, “Influence of powder feed parameters on the powder stream in laser metal deposition (LMD) by high-speed and high-resolution imaging, LAF 2022: Proceedings of the 12th laser applications forum,” in *Strahltechnik Band 76*, edited by T. Seefeld, T. Radel, and T. Mattulat (BIAS Verlag, Bremen, 2022), pp. 1–6.
- ¹⁴G. Wang, Y. Qin, and S. Yang, “Characterization of laser-powder interaction and particle transport phenomena during laser direct deposition of W–Cu composite,” *Add. Manuf.* **37**, 101722 (2021).
- ¹⁵A. Ebrahimi, M. Sattari, S. J. Bremer, M. Luckabauer, G. R. Römer, I. M. Richardson, C. R. Kleijn, and M. J. Hermans, “The influence of laser characteristics on internal flow behaviour in laser melting of metallic substrates,” *Mater. Des.* **214**, 110385 (2022).
- ¹⁶A. Aggarwal, A. Chouhan, S. Patel, D. K. Yadav, A. Kumar, A. R. Vinod, K. G. Prashanth, and N. P. Gurao, “Role of impinging powder particles on melt pool hydrodynamics, thermal behaviour and microstructure in laser-assisted DED process: A particle-scale DEM–CFD–CA approach,” *Int. J. Heat Mass Transfer* **158**, 119989 (2020).
- ¹⁷H. Wang, F. E. Pfefferkorn, and S. J. Wolff, “Investigation of pore formation mechanisms induced by spherical-powder delivery in directed energy deposition using in situ high-speed x-ray imaging,” *Addit. Manuf. Lett.* **3**, 100050 (2022).

¹⁸J. Volpp, "Behavior of powder particles on melt pool surfaces," *Int. J. Adv. Manuf. Technol.* **102**, 2201–2210 (2019).

¹⁹A. Bohlen, T. Seefeld, A. Haghsheenas, and R. Groll, "Characterization of the powder stream propagation behavior of a discrete coaxial nozzle for laser metal deposition," *J. Laser Appl.* **34**, 42048 (2022).

²⁰A. Bohlen, D. Tyralla, and T. Seefeld, "Characterization method for different powder nozzle types used in laser metal deposition," in *Proceedings of Lasers in*

Manufacturing Conference 2023 (LiM 2023), Munich, Germany, 26–29 June 2023 [Hannover, German Scientific Laser Society/Wissenschaftliche Gesellschaft Lasertechnik e.V. (WLT e.V.), 2023].

²¹J.-Y. Tinevez, N. Perry, J. Schindelin, G. M. Hoopes, G. D. Reynolds, E. Laplantine, S. Y. Bednarek, S. L. Shorte, and K. W. Eliceiri, "Trackmate: An open and extensible platform for single-particle tracking," *Methods* **115**, 80–90 (2017).